

Hot Deformation Characteristics and Processing Maps of the Cu-Cr-Zr-Ag Alloy

Yi Zhang, Zhe Chai, Alex A. Volinsky , Huili Sun, Baohong Tian, Ping Liu, and Yong Liu

(Submitted October 26, 2015; in revised form January 10, 2016; published online February 8, 2016)

The hot deformation behavior of the Cu-Cr-Zr-Ag alloy has been investigated by hot compressive tests in the 650–950 °C temperature and 0.001–10 s⁻¹ strain rate ranges using Gleeble-1500D thermo-mechanical simulator. The microstructure evolution of the alloy during deformation was characterized using optical and transmission electron microscopy. The flow stress decreases with the deformation temperature and increases with the strain rate. The apparent activation energy for hot deformation of the alloy was 343.23 kJ/mol. The constitutive equation of the alloy based on the hyperbolic-sine equation was established to characterize the flow stress as a function of the strain rate and the deformation temperature. The processing maps were established based on the dynamic material model. The optimal processing parameters for hot deformation of the Cu-Cr-Zr-Ag alloy are 900–950 °C and 0.001–0.1 s⁻¹ strain rate. The evolution of DRX microstructure strongly depends on the deformation temperature and the strain rate.

Keywords constitutive equation, Cu-Cr-Zr-Ag alloy, dynamic recrystallization, hot deformation behavior, processing maps

1. Introduction

High strength and high conductivity copper alloys are very important in the electronics industry. These materials are widely used as electric railway and switch contacts, casting molds, high-pulsed magnetic field conductors, electric vehicle motors, and lead frames (Ref 1–3). The lead frame is the foundation of the integrated circuits, which plays the main role of supporting the chip, along with electrical signal transmission and heat dissipation in the integrated circuit. Initially, Kovar and Fe-Ni₄₂ alloys were used in the lead frame, followed by Cu-Fe, Cu-P, and Cu-Fe-P alloys. Due to the high electrical conductivity, Cu-Cr-Zr alloys are now widely used as the lead frame materials (Ref 4–6).

Previous reports have mainly focused on cold worked or thermally treated alloys, dealing with properties, applications,

microstructure, and phases of the Cu-Cr-Zr alloy. For instance, Bi et al. (Ref 7) studied the phases and the as-cast structure of the Cu-15%Cr-0.24%Zr alloy. It was found that there were four types of phases, namely, the Cu matrix, Cr dendrite, eutectic Cr, and the coarse Zr-rich phase. Su et al. (Ref 8) studied the Cu-Cr-Zr-Mg alloys aged at 470 °C. It was found that the alloy aged at 470 °C had fine precipitation of CrCu₂(Zr, Mg), Cr, and Cu₄Zr phases. Mu et al. (Ref 9) studied the Cu-Cr-Zr-Mg-RE alloy, and three kinds of precipitates were observed: chromium-rich, zirconium-rich, and the Heusler phases. Similar results were obtained by Xia et al. (Ref 10). However, the hot deformation behavior and precipitation transformation mechanisms of the Cu-Cr-Zr alloy are uncertain. In order to optimize the hot workability of the Cu-Cr-Zr alloy, hot deformation behavior, strain-hardening rate, and processing maps of the Cu-Cr-Zr alloys were investigated in this study.

This study aims to evaluate the flow behavior of the Cu-Cr-Zr-Ag alloy by hot compression tests under various deformation conditions and to analyze the deformation mechanisms using microstructure observations. The constitutive constants of this alloy have been determined, and constitutive equations relating the *Z* parameter and hot deformation activation energy, *Q*, have been derived in this alloy. The optimal hot deformation processing parameters of this alloy were established by the processing maps. Furthermore, the DRX nucleation mechanisms based on the microstructure evolution during hot compression are also discussed.

2. Experimental Procedure

The experimental alloy was melt in a vacuum induction furnace under argon atmosphere and then cast into the Φ 83 × 150 mm² low-carbon steel mold. Its chemical composition is as follows (wt.%): 0.8Cr, 0.3Zr, 0.2Ag, and balance Cu. The ingot was homogenized at 930 °C for 2 h to remove the segregation of the alloying elements. Subsequently, the ingot was forged into bars with 25-mm diameter. Finally, the forged bars were solution-treated at 900 °C for 1 h, followed by water quenching.

Yi Zhang, School of Materials Science and Engineering, Henan University of Science and Technology, Luoyang 471003, China; Department of Mechanical Engineering, University of South Florida, Tampa 33620; and Collaborative Innovation Center of Nonferrous Metals, Luoyang 471003 Henan Province, China; **Zhe Chai**, School of Materials Science and Engineering, Henan University of Science and Technology, Luoyang 471003, China and School of Materials Science and Engineering, University of Shanghai for Science and Technology, Shanghai 200093, China; **Alex A. Volinsky**, Department of Mechanical Engineering, University of South Florida, Tampa 33620; **Huili Sun**, **Baohong Tian**, and **Yong Liu**, School of Materials Science and Engineering, Henan University of Science and Technology, Luoyang 471003, China and Collaborative Innovation Center of Nonferrous Metals, Luoyang 471003 Henan Province, China; and **Ping Liu**, School of Materials Science and Engineering, University of Shanghai for Science and Technology, Shanghai 200093, China. Contact e-mails: zhshgu436@163.com, volinsky@eng.usf.edu and volinsky@usf.edu.

The hot compression specimens were cut into a cylindrical shape with a diameter of 8 mm and length of 12 mm. The hot compression tests were carried out on the Gleeble-1500D thermo-simulator at a strain rate of $0.001\text{--}10\text{ s}^{-1}$ and deformation temperature of $650\text{--}950\text{ }^{\circ}\text{C}$. The specimens were heated to deformation temperature at the rate of $5\text{ }^{\circ}\text{C/s}$. Before deformation, all specimens were kept at the deformation temperature for 180 s in order to homogenize the temperature. The accuracy of temperature control was $\pm 0.5\text{ }^{\circ}\text{C}$. The yield stress standard deviation for the performed measurements was $\pm 3\text{ MPa}$. The standard deviation meets the ASTM-E8 standard and the error bars for the yield stress are less than $\pm 1.5\%$. All specimens were compressed and immediately water-quenched from the test temperature to maintain deformation microstructure. The deformed specimens were sectioned through the longitudinal axis. All specimens were polished and then etched with a solution of FeCl_3 (5 g) + $\text{C}_2\text{H}_5\text{OH}$ (85 mL) + HCl (10 mL).

The microstructure was observed using OLYMPUS PMG3 optical microscope. Transmission electron microscopy (TEM) samples were prepared using Gatan 691 ion beam thinner. The precipitated phase was characterized using JEM-2100 (Jeol, Japan) high-resolution transmission electron microscope (HRTEM).

3. Results and Discussion

3.1 Flow Stress Behavior

The flow stress curves of the Cu-Cr-Zr-Ag alloy at various strain rates and deformation temperatures are shown in Fig. 1. The flow stress of the Cu-Cr-Zr-Ag alloy is strongly affected by the strain rate and deformation temperature. Under a certain strain rate, the higher the deformation temperature, the lower

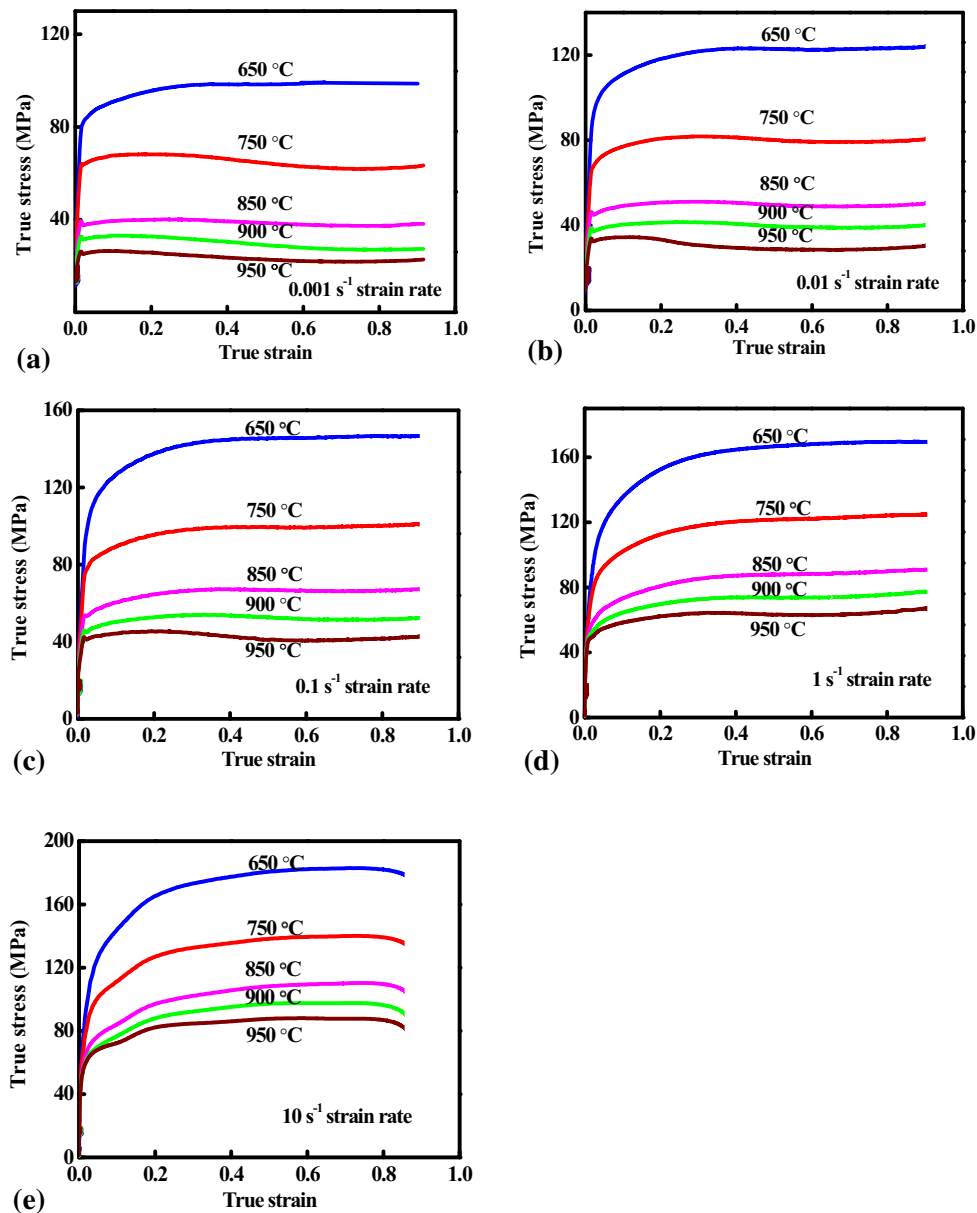


Fig. 1 True stress-strain curves of the Cu-Cr-Zr-Ag alloy deformed at different temperatures and strain rates: (a) $\dot{\epsilon} = 0.001\text{ s}^{-1}$; (b) $\dot{\epsilon} = 0.01\text{ s}^{-1}$; (c) $\dot{\epsilon} = 0.1\text{ s}^{-1}$; (d) $\dot{\epsilon} = 1\text{ s}^{-1}$; (e) $\dot{\epsilon} = 10\text{ s}^{-1}$

the flow stress. Under a certain deformation temperature, higher strain rate leads to the larger flow stress. It can be seen from Fig. 2(a) that during the compression test at 650 °C and 0.001 s⁻¹, continuous strain hardening was observed over the entire deformation range. However, most of the true stress-strain curves exhibit a maximum stress, known as the peak stress, followed by a decrease in the stress, finally reaching a plateau. For example, the flow curve of the sample deformed at 950 °C and 0.001 s⁻¹ belongs to this type. This means that there is enough time for the softening or dislocation annihilation at a low strain rate, while the atomic kinetic energy and the atomic vibration amplitude of the Cu-Cr-Zr-Ag alloy increase at high deformation temperature, which also improves the coordination of the grains and eventually leads to the increase in the plasticity and the decrease in the strength.

3.2 Constitutive Analysis

In hot working, the constitutive relationship between the flow stress, strain rate and deformation temperature can be expressed as (Ref 11-15):

$$\dot{\epsilon} = A_1 \sigma^{n_1} \exp\left(-\frac{Q}{RT}\right) \quad (\text{Eq 1})$$

$$\dot{\epsilon} = A_2 \exp(\beta\sigma) \exp\left(-\frac{Q}{RT}\right) \quad (\text{Eq 2})$$

$$\dot{\epsilon} = A[\sinh(\alpha\sigma)]^n \exp\left(-\frac{Q}{RT}\right) \quad (\text{Eq 3})$$

$$Z = \dot{\epsilon} \exp\left(\frac{Q}{RT}\right). \quad (\text{Eq 4})$$

Here, $\dot{\epsilon}$ is the strain rate, Q is the activation energy of DRX, R is the universal gas constant, T is the absolute temperature, σ is the flow stress for a given strain, and A , A_1 , A_2 , n_1 , n , and α are the materials constants ($\alpha = \beta/n_1$). Taking natural logarithms on both sides of Eq 1 and 2 yields

$$\ln \dot{\epsilon} = \ln A_1 + n_1 \ln \sigma - Q/RT \quad (\text{Eq 5})$$

$$\ln \dot{\epsilon} = \ln A_2 + \beta\sigma - Q/RT \quad (\text{Eq 6})$$

A linear relationship exists between $\ln \dot{\epsilon}$ and $\ln \sigma$ with linear slope n_1 shown in Fig. 2(a). A linear relationship exists between $\ln \dot{\epsilon}$ and σ with linear slope β shown in Fig. 2(b). The values of n_1 and β can be calculated from the average values of the slopes: $n = 7.715$ and $\beta = 0.0849$. Thus, the α value of the alloy is calculated as $\alpha = \beta/n = 0.011 \text{ MPa}^{-1}$.

Taking natural logarithms on both sides of Eq 3 yields

$$\ln[\sinh(\alpha\sigma)] = \frac{1}{n} \ln \dot{\epsilon} + \frac{Q}{nR} \left(\frac{1}{T}\right) - \frac{1}{n} \ln A \quad (\text{Eq 7})$$

If $\dot{\epsilon}$ is a constant, the Eq 7 can be written as follows:

$$Q = R \left[\frac{\partial(\ln \dot{\epsilon})}{\partial \ln[\sinh(\alpha\sigma)]} \right]_T \left[\frac{\partial \ln[\sinh(\alpha\sigma)]}{\partial (1/T)} \right]_{\dot{\epsilon}} = RnS \quad (\text{Eq 8})$$

where n and S are the slopes of the plots of $\ln \dot{\epsilon}$ versus $\ln[\sinh(\alpha\sigma)]$ at constant temperature and $\ln[\sinh(\alpha\sigma)]$ versus $1000/T$ at constant strain rate, respectively. It can be found that there exists a good linear relationship between $\ln \dot{\epsilon}$ and $\ln[\sinh(\alpha\sigma)]$ when T remains constant, and $\ln[\sinh(\alpha\sigma)]$ is linear with $(1000/T)$ when $\dot{\epsilon}$ remains constant, as shown in Fig. 3(a)

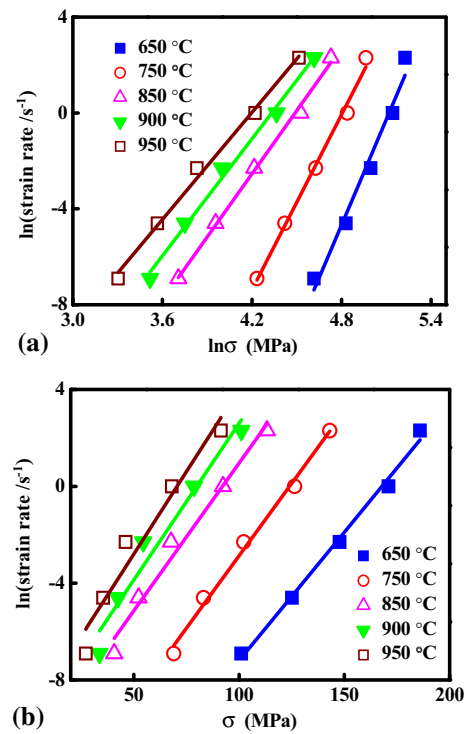


Fig. 2 Relationships between: (a) $\ln \dot{\epsilon}$ and $\ln \sigma$; (b) $\ln \dot{\epsilon}$ and σ

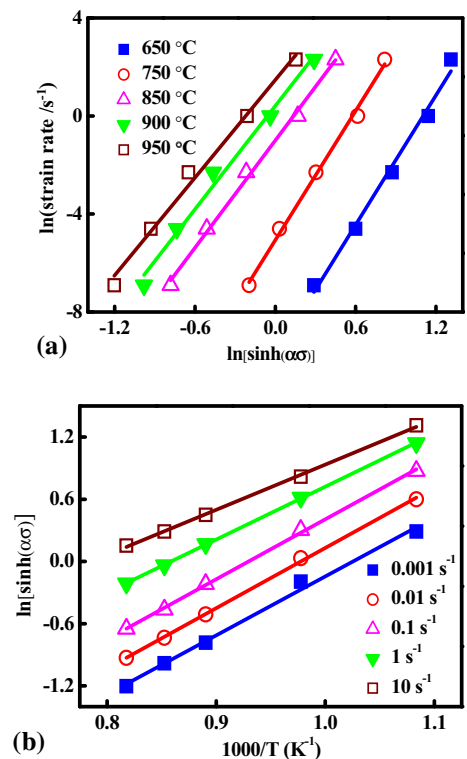


Fig. 3 Relationship between (a) $\ln[\sinh(\alpha\sigma)]$ and $\ln \dot{\epsilon}$; (b) $\ln[\sinh(\alpha\sigma)]$ and $1000/T$

and (b), respectively. Then the values of n and S can be determined as 7.715 and 5.472 by means of linear regression analysis. Consequently, the value of Q for the experimental alloy is 343.23 kJ/mol.

The high Q value of 343.23 kJ/mol indicates that the flow stress in this alloy is highly temperature dependent. According to Eq 4, the relationship between $\ln[\sinh(\alpha\sigma)]$ and $\ln Z$ for the Cu-Cr-Zr-Ag is

$$\ln Z = \ln A + n \ln[\sinh(\alpha\sigma)]. \quad (\text{Eq 9})$$

Figure 4 illustrates that the experimental data of the flow stress at different hot deformation conditions are well fitted with the hyperbolic-sine function. Thus, the constitutive equation of the Cu-Cr-Zr-Ag alloy in the hyperbolic-sine function can be expressed as follows:

$$\dot{\epsilon} = e^{35.82} [\sinh(0.011\sigma)]^{7.72} \exp(-343.23/RT) \quad (\text{Eq 10})$$

The Q value of this alloy is a little lower than of the Cu-0.4Cr-0.15Zr-0.05Ce alloy (495.8 kJ/mol) (Ref 16), the Cu-0.36Cr-

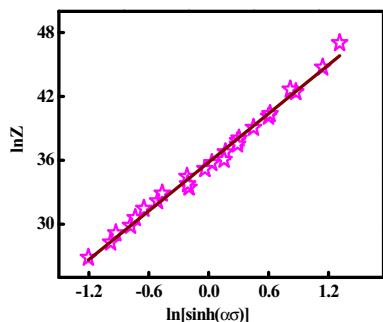


Fig. 4 The Zener-Hollomon parameter, Z , as a function of the flow stress

0.03Zr alloy (432.6 kJ/mol) (Ref 17), and the Cu-0.6Cr-0.03Zr alloy (572.053 kJ/mol) (Ref 18). The reason is because Ag has similar crystal structure and electronegativity as Cu. Compared with the above references, the addition of Ag can refine the grain of the Cu-Cr-Zr alloy. Due to the refinement effect of Ag addition, the DRX nucleation is improved by increasing the grain boundary area. The addition of Ag can also increase the accumulated energy and the formation of high dislocation density. Therefore, the existence of accumulated energy and dislocations improves the driving force for recrystallized nucleation. The higher the activation energy Q , the harder is the alloy hot deformation (Ref 19). This indicates that dislocation movement and DRX are easier to occur for this experimental alloy. It also means that this experimental alloy has good hot workability.

3.3 Characterization of the Processing Maps

The processing map technique has been used earlier to study the hot deformation mechanisms in Mg and its alloys by Prasad and Srinivasan (Ref 20). In this model, it is considered that the work piece undergoing hot deformation is the dissipater of power, and the instantaneous power dissipated can be separated into two complementary parts: the G content (temperature rise) and the J content (microstructure mechanisms). The total dissipated power, therefore, can be written as in (Ref 21, 22):

$$P = \sigma \dot{\epsilon} = \int_0^{\sigma} \dot{\epsilon} d\sigma + \int_0^{\dot{\epsilon}} \sigma d\dot{\epsilon} \quad (\text{Eq 11})$$

where $G = \int_0^{\dot{\epsilon}} \sigma d\dot{\epsilon}$, $J = \int_0^{\sigma} \dot{\epsilon} d\sigma$, and $P = G + J$. Here, $\dot{\epsilon}$ is the strain rate and σ is the flow stress.

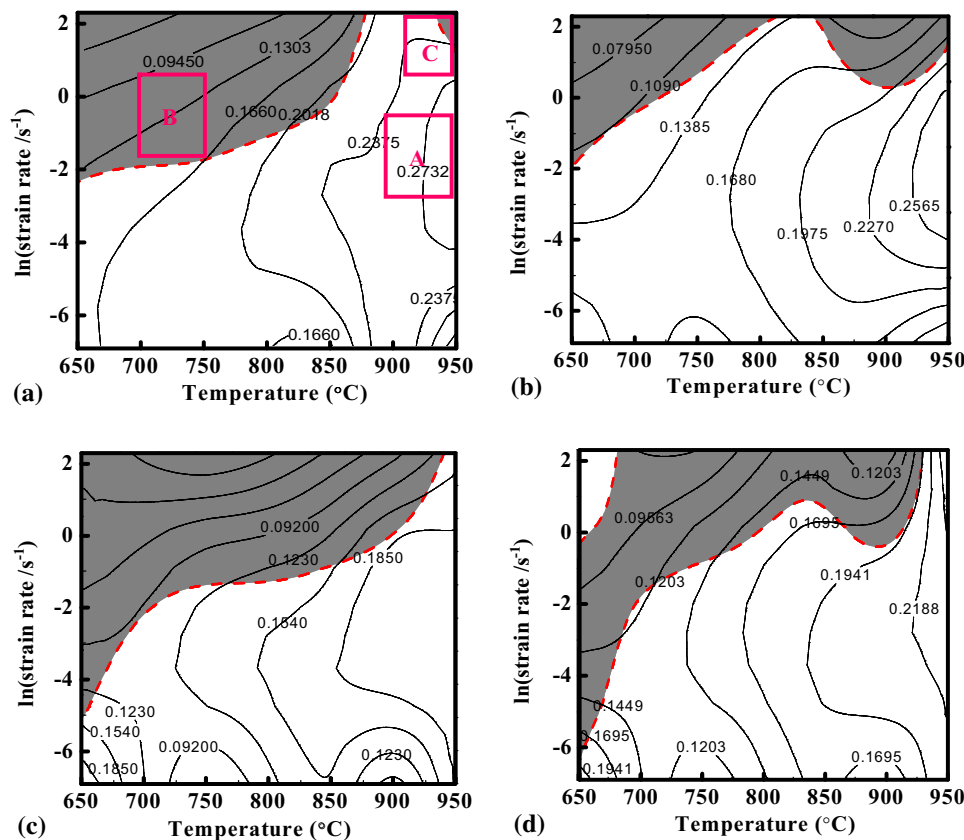


Fig. 5 Processing maps of the Cu-Cr-Zr-Ag alloy at a true strain of: (a) 0.3, (b) 0.4, (c) 0.5, and (d) 0.6

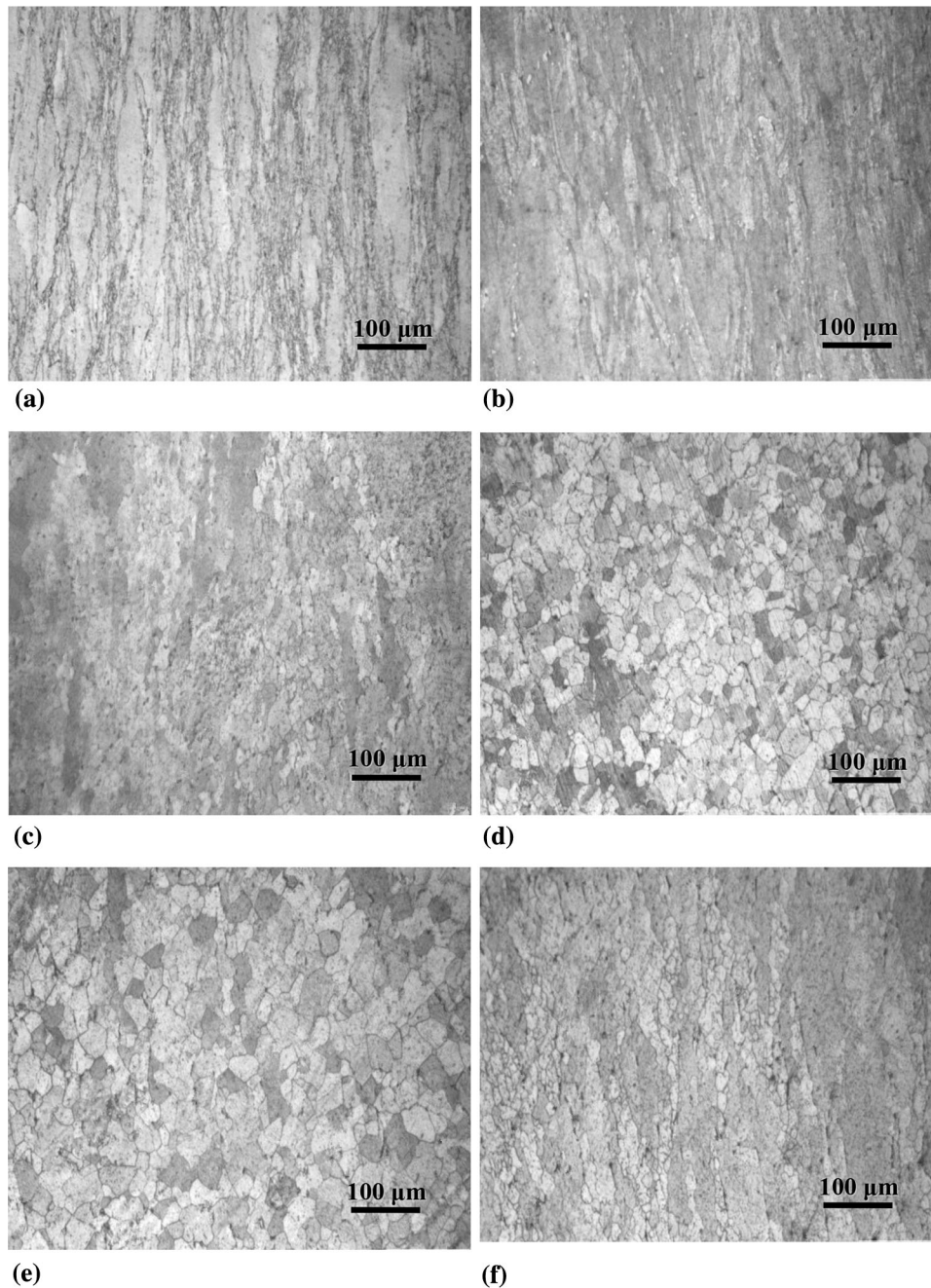


Fig. 6 Microstructure of the Cu-Cr-Zr-Ag alloy hot deformed to 0.3 strain and different conditions: (a) 650 °C and 10 s^{-1} , (b) 750 °C and 0.1 s^{-1} , (c) 850 °C and 0.001 s^{-1} , (d) 900 °C and 0.1 s^{-1} , (e) 950 °C and 0.001 s^{-1} , and (f) 950 °C and 10 s^{-1}

The power dissipation capacity of the material can be evaluated by the efficiency of power dissipation, η , which is given by the strain rate sensitivity parameter, m (Ref 23, 24):

$$\eta = \frac{J}{J_{\max}} = \frac{2m}{m+1} \quad (\text{Eq 12})$$

where m is the strain rate sensitivity of the flow stress, described as follows:

$$m = \frac{dJ}{dG} = \left[\frac{\partial(\ln \sigma)}{\partial(\ln \dot{\epsilon})} \right]_{\epsilon, T} \quad (\text{Eq 13})$$

which is a function of the deformation temperature and the strain rate.

Further, the extremum principles of irreversible thermodynamics as applied to continuum mechanics of large plastic flow are explored to define a criterion for the onset of flow instability using the instability parameter (Ref 25):

$$\zeta(\dot{\epsilon}) = \frac{\partial \ln \left(\frac{m}{m+1} \right)}{\partial \ln \dot{\epsilon}} + m < 0. \quad (\text{Eq 14})$$

The variation of $\zeta(\dot{\epsilon})$ with temperature and the strain rate constitutes the instability map, which can be superimposed on the processing map to delineate instability regimes of the negative $\zeta(\dot{\epsilon})$ values.

The processing map of the Cu-Cr-Zr-Ag alloy deformed at the strain of 0.3, 0.4, 0.5, and 0.6 is obtained in Fig. 5, where

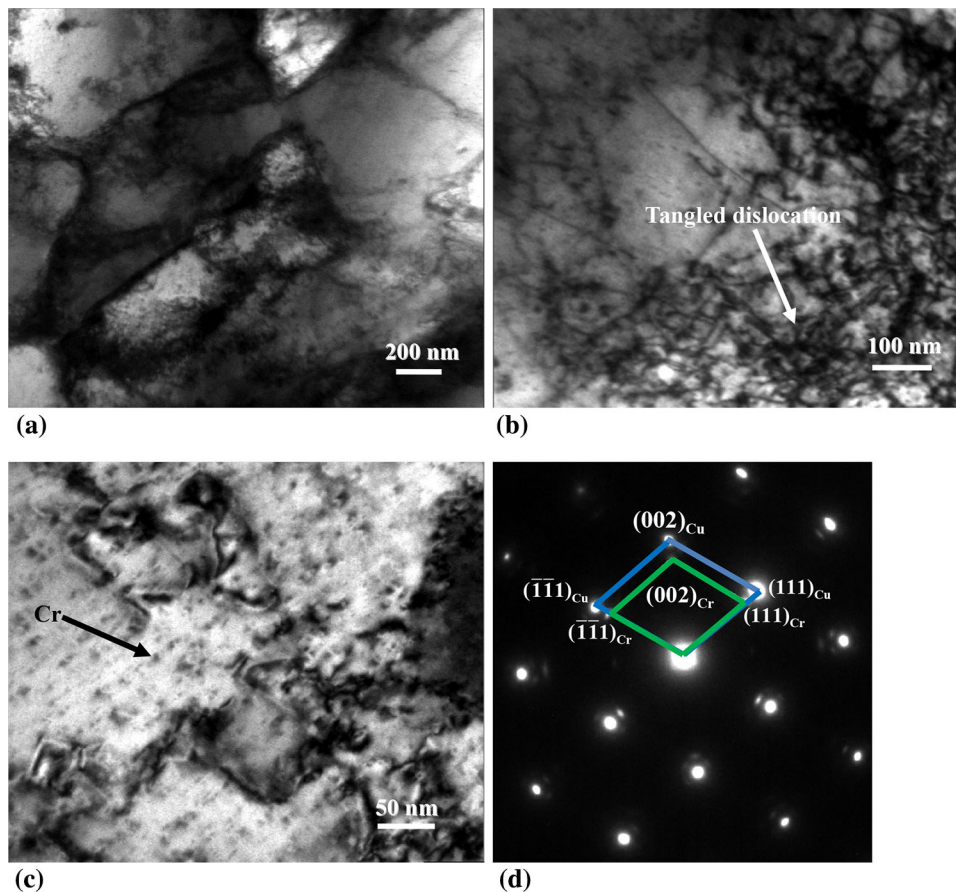


Fig. 7 Transmission electron micrographs of the Cu-Cr-Zr-Ag alloy deformed at (a) 650 °C and 10 s^{-1} , (b) 750 °C and 0.1 s^{-1} , (c) 900 °C and 0.1 s^{-1} , and (d) SAED pattern for (c)

the unstable region is represented by the shaded domains and the contour lines express the efficiency of power dissipation. With the increase of deformation temperature or the decrease of strain rate, efficiency of power dissipation increases. At the strain of 0.3, the maps exhibit three domains. Domain A represents a stable region with a peak efficiency of power dissipation shown in Fig. 5(a). It revealed a greater efficiency of power dissipation in the temperature range of 900-950 °C and the strain rate range of $0.1\text{-}1 \text{ s}^{-1}$, with a peak efficiency of about 27.3% at 930 °C and 0.1 s^{-1} . This indicates that domains with a higher efficiency of power dissipation commonly represent optimal processing conditions (Ref 26). Domain B occurs in the temperature range of 650-870 °C and the strain rate range of $0.1\text{-}10 \text{ s}^{-1}$. It can be seen that this region is at the lower temperature and higher strain rate conditions. Some very low values of power dissipation efficiency were observed. It is often considered to be the instability region. The domain C occurs in the temperature range of 940-950 °C and the strain rate range of $5\text{-}10 \text{ s}^{-1}$, which is also in the high strain rate region. In this instability region, many research results indicate that the hot workability of the alloy in the high strain rate region becomes inferior (Ref 27). It is generally accepted that the flow instability is associated with localized shear initiated by high strain rates (Ref 28). Thus, hot working in these regions is also considered to be unsafe. When the strain is 0.4, the processing maps exhibited two unstable domains in the following temperature and strain rate ranges: one in the 650-800 °C deformation

temperature and $0.01\text{-}10 \text{ s}^{-1}$ strain rate ranges, and another is in the 850-950 °C deformation temperature and $1\text{-}10 \text{ s}^{-1}$ strain rate ranges, as shown in Fig. 5(b). When the strain is 0.5 and 0.6, similar shaded domains were observed at the strain rate of $1\text{-}10 \text{ s}^{-1}$, as shown in Fig. 5(c) and (d). It can be seen that these two domains occur at low temperature and high strain rate. High dislocation density areas easily form around solute atoms at high strain rate (Ref 29). At the same time, the lattice distorts near the interface, creating a stresses concentration. When the local stress exceeds the alloy strength, many cracks form along the grain boundaries, causing fracture. During practical applications, it is necessary to stay away from this domain and the corresponding processing parameters. By means of the modified processing map developed in Fig. 5, the optimized conditions for hot deformation of the studied Cu-Cr-Zr-Ag alloy can be proposed as 900-950 °C temperature range and $0.001\text{-}0.1 \text{ s}^{-1}$ strain rate.

3.4 Microstructure Observations

The microstructure evolution during hot deformation was characterized by optical microscopy to validate the regions of stable and unstable flow, and to find a practical relation between the final microstructure and processing variables. Figure 6 shows typical microstructure of the Cu-Cr-Zr-Ag alloy deformed at 0.3 strain and different deformation conditions. The optical image of the Cu-Cr-Zr-Ag alloy microstructure

deformed at 650 and 750 °C with the strain rate of 10 and 0.1 s⁻¹ is shown in Fig. 6(a) and (b), respectively. There is only the shear zone present with no dynamic recrystallization grains found. This means that the main softening mechanism is dynamic recovery in the domain B. The alloy produced local temperature rise by local plastic deformation at high strain rate and low temperature, so it can easily fracture during deformation processing (Ref 25, 30). Thus, these conditions should be avoided in industrial practice. The microstructure of the Cu-Cr-Zr-Ag alloy deformed at 850 °C with the strain rate of 0.001 s⁻¹ is shown in Fig. 6(c). It can be seen that the microstructure has mixed small dynamic recrystallized and elongated grains. Under these deformation conditions, the alloy is unstable. For practical applications, it is also necessary to stay away from this microstructure. With the increasing temperature, the specimen deformed in the domain A exhibits complete DRX structure as shown in Fig. 6(d). The microstructure of the deformed alloy shows complete recrystallization with uniform and fine grains. Comparing Fig. 6(d) and (e), the DRX grains deformed at 950 °C and 0.001 s⁻¹ obviously grow in size, but the DRX grains are still fine and homogenized. When deformed at high temperature and low strain rate, the DRX grains have larger driving force for nucleation and growth (Ref 31). The microstructure of the specimen deformed at the strain rate of 10 s⁻¹ and 950 °C (domain C) is shown in Fig. 6(f). Some recrystallized grains around original grain boundaries and some elongated grains are observed. This microstructure is often called mixed-grain microstructure (Ref 32), and is unstable during hot deformation. Finally, it can be concluded that the optimal processing parameters for hot deformation of the Cu-Cr-Zr-Ag alloy are 900-950 °C and 0.001-0.1 s⁻¹ strain rate.

Figure 7 shows the TEM microstructure of the Cu-Cr-Zr-Ag alloy deformed at various deformation conditions. It can be seen that the grains are elongated in Fig. 7(a). Figure 7(b) shows that the dislocations are tangled and stored in the grain interiors with the Cu-Cr-Zr-Ag alloy deformed at 750 °C with the strain rate of 0.1 s⁻¹. Due to the dislocation strengthening, the flow stress and work-hardening rate increase with the decrease of deformation temperature. The rapid increase of the number of dislocations easily induces dynamic recrystallization once the dislocation density exceeds a critical value (Ref 33). Figure 7(c) shows typical microstructure of the Cu-Cr-Zr-Ag alloy, indicating the occurrence of DRX. Figure 7(d) shows the selected area electron diffraction (SAED) pattern. It indicated that the precipitates are chromium-rich particles. The fine chromium-rich particles are distributed in the matrix. Many dislocations pile up and jam around the chromium-rich particles, increasing the amount of accumulated energy in the regions. After that, it can effectively increase the dislocation density and the nucleation of DRX. Finally, the dispersed secondary phase of Cr particles produces great resistance to the shift of boundaries, and growth of recrystallized grains is suppressed.

4. Conclusions

Hot compression tests of the Cu-Cr-Zr-Ag alloy were performed using the Gleeble-1500D system in the 650-950 °C temperature and 0.001-10 s⁻¹ strain rate ranges. Based on the results, the following conclusions can be drawn:

- (1) The flow stress of the Cu-Cr-Zr-Ag alloy increases with the increasing strain rate and decreasing deformation temperature. The constitutive relationship between the peak stress, strain rate, and deformation temperature can be described by the Z parameter in the hyperbolic-sine function with the hot deformation activation energy of $Q = 343.23$ kJ/mol. The constitutive equation of the Cu-Cr-Zr-Ag alloy can be expressed as follows: $\dot{\epsilon} = e^{35.82} [\sinh(0.011\sigma)]^{7.72} \exp(-343.23/RT)$.
- (2) Through processing map, the optimized conditions for hot deformation of the Cu-Cr-Zr-Ag alloy can be proposed at the 900-950 °C temperature and 0.001-0.1 s⁻¹ and strain rate ranges.
- (3) The deformation temperature and strain rate can strongly affect the deformed microstructure. Dynamic recrystallization appears at high temperature and low strain rate.

Acknowledgments

This work was supported by the National Natural Science Foundation of China (No. 51101052) and by the National Science Foundation (IRES 1358088). The authors would like to thank an anonymous reviewer for useful comments.

References

1. P. Liu, B.X. Kang, X.G. Cao, J.L. Huang, B. Yen, and H.C. Gu, Aging Precipitation and Recrystallization of Rapidly Solidified Cu-Cr-Zr-Mg Alloy, *Mater. Sci. Eng. A.*, 1999, **265**, p 262-267
2. D.M. Zhao, Q.M. Dong, P. Liu, B.X. Kang, J.L. Huang, and Z.H. Jin, Structure and Strength of the Age Hardened Cu-Ni-Si Alloy, *Mater. Chem. Phys.*, 2003, **79**, p 81-86
3. S.C. Krishna, N.K. Gangwar, A.K. Jha, B. Pant, and K.M. George, Enhanced Strength in Cu-Ag-Zr Alloy by Combination of Cold Working and Aging, *J. Mater. Eng. Perform.*, 2014, **23**, p 1458-1464
4. H. Zhang, H.G. Zhang, and L.X. Li, Hot Deformation Behavior of Cu-Fe-P Alloys During Compression at Elevated Temperatures, *J. Mater. Process. Technol.*, 2009, **209**, p 2892-2896
5. G.B. Lin, Z.D. Wang, M.K. Zhang, H. Zhang, and M. Zhao, Heat Treatment Method for Making High Strength and Conductivity Cu-Cr-Zr Alloy, *Mater. Sci. Technol.*, 2011, **27**, p 966-969
6. S.G. Jia, P. Liu, F.Z. Ren, and M.S. Zheng, Wear Behavior of Cu-Ag-Cr Alloy Wire Under Electrical Sliding, *Mater. Sci. Eng. A*, 2005, **398**, p 166-262
7. L.M. Bi, P. Liu, X.H. Chen, X.K. Liu, W. Li, and F.C. Ma, Analysis of Phase in Cu-15%Cr-0.24%Zr Alloy, *Trans. Nonferr. Met. Soc. China*, 2013, **23**, p 1342-1348
8. J.H. Su, Q.M. Dong, P. Liu, H.J. Li, and B.X. Kang, Research on Aging Precipitation in a Cu-Cr-Zr-Mg Alloy, *Mater. Sci. Eng. A.*, 2005, **392**, p 422-426
9. S.G. Mu, F.A. Guo, Y.Q. Tang, X.M. Cao, and M.T. Tang, Study on Microstructure and Properties of Aged Cu-Cr-Zr-Mg-RE Alloy, *Mater. Sci. Eng. A*, 2008, **475**, p 235-240
10. C.D. Xia, Y.L. Jia, W. Zhang, K. Zhang, Q.Y. Dong, G.Y. Xu, and M. Wang, Study of Deformation and Aging Behaviors of a Hot Rolled-Quenched Cu-Cr-Zr-Mg-Si Alloy During Thermomechanical Treatments, *Mater. Des.*, 2012, **39**, p 404-409
11. A. Momeni, H. Arabi, A. Rezaei, H. Badri, and S.M. Abbasi, Hot Deformation Behavior of Austenite in HSLA-100 Microalloyed Steel, *Mater. Sci. Eng. A*, 2011, **528**, p 2158-2163
12. C.M. Sellars and W.J. McTegart, On the Mechanism of Hot Deformation, *Acta Metall.*, 1966, **14**, p 1136-1138
13. M.R. Rokni, A. Zarei-Hanzaki, A.A. Roostaei, and H.R. Abedi, An Investigation into the Hot Deformation Characteristics of 7075 Aluminum Alloy, *Mater. Des.*, 2011, **32**, p 2339-2344
14. S. Banerjee, P.S. Robi, and A. Srinivasan, Deformation Processing Maps for Control of Microstructure in Al-Cu-Mg Alloys Microalloyed with Sn, *Metall. Mater. Trans. A*, 2012, **43**, p 3834-3849

15. M. Rajamuthamilselvan and S. Ramanathan, Hot Deformation Behaviour of 7075 Alloy, *J. Alloys Compd.*, 2011, **509**, p 948–952
16. Y. Zhang, A.A. Volinsky, H.T. Tran, Z. Chai, P. Liu, and B.H. Tian, Effects of Ce Addition on High Temperature Deformation Behavior of Cu-Cr-Zr Alloys, *J. Mater. Eng. Perform.*, 2015, **24**, p 3783–3788
17. G.L. Ji, Q. Li, K.Y. Ding, L. Yang, and L. Li, A Physically-Based Constitutive Model for High Temperature Deformation of Cu-0.36Cr-0.03Zr Alloy, *J. Alloys Compd.*, 2015, **648**, p 397–407
18. Z.Y. Ding, S.G. Jia, P.F. Zhao, M. Deng, and K.X. Song, Hot Deformation Behavior of Cu-0.6Cr-0.03Zr Alloy During Compression at Elevated Temperatures, *Mater. Sci. Eng. A*, 2013, **570**, p 87–91
19. H.J. McQueen, S. Yue, N.D. Ryan, and E. Fry, Hot Working Characteristics of Steels in Austenitic State, *J. Mater. Process. Technol.*, 1995, **53**, p 293–310
20. Y.V.R.K. Prasad and P.R. Rao, Processing Maps for Hot Deformation of Rolled AZ31 Magnesium Alloy Plate: Anisotropy of Hot Workability, *Mater. Sci. Eng. A*, 2012, **487**, p 316–327
21. X.S. Xia, Q. Chen, K. Zhang, Z.D. Zhao, M.L. Ma, X.G. Li, and Y.J. Li, Hot Deformation Behavior and Processing Map of Coarse-Grained Mg-Gd-Y-Nd-Zr Alloy, *Mater. Sci. Eng. A*, 2013, **587**, p 283–290
22. N. Srinivasan, Y.V.R.K. Prasad, and P.R. Rao, Hot deformation Behaviour of Mg-3Al Alloy—A Study Using Processing Map, *Mater. Sci. Eng. A*, 2008, **476**, p 146–156
23. N.P. Jin, H. Zhang, Y. Han, and W.X. Wu, Hot Deformation Behavior of 7150 Aluminum Alloy During Compression at Elevated Temperature, *Mater. Charact.*, 2009, **60**, p 530–536
24. L. Li and X.M. Zhang, Hot Compression Deformation Behavior and Processing Parameters of a Cast Mg-Gd-Y-Zr Alloy, *Mater. Sci. Eng. A*, 2011, **528**, p 1396–1401
25. T. Xi, C.G. Yang, M.B. Shahzad, and K. Yang, Study of the Processing Map and Hot Deformation Behavior of a Cu-Bearing 317LN Austenitic Stainless Steel, *Mater. Des.*, 2015, **87**, p 303–312
26. H. Mirzadeh, Constitutive Description of 7075 Aluminum Alloy During Hot Deformation by Apparent and Physically-Based Approaches, *J. Mater. Eng. Perform.*, 2015, **24**, p 1095–1099
27. L. Wang, F. Liu, J.J. Cheng, Q. Zuo, and C.F. Chen, Hot Deformation Characteristics and Processing Map Analysis for Nickel-Based Corrosion Resistant Alloy, *J. Alloys Compd.*, 2015, **623**, p 69–78
28. H.Y. Zhan, W.D. Zeng, G. Wang, D. Kent, and M. Dargusch, Microstructural Characteristics of Adiabatic Shear Localization in a Metastable Beta Titanium Alloy Deformed at High Strain Rate and Elevated Temperatures, *Mater. Charact.*, 2015, **102**, p 103–113
29. D.J. Li, Y.R. Feng, Z.F. Yin, F.S. Shangguan, K. Wang, Q. Liu, and F. Hu, Prediction of Hot Deformation Behaviour of Fe-25Mn-3Si-3Al TWIP steel, *Mater. Sci. Eng. A*, 2011, **528**, p 8084–8089
30. Y. Sun, W.D. Zeng, Y.Q. Zhao, X.M. Zhang, Y. Shu, and Y.G. Zhou, Research on the Hot Deformation Behavior of Ti40 Alloy Using Processing Map, *Mater. Sci. Eng. A*, 2011, **528**, p 1205–1211
31. Y.Y. Chen, B.H. Li, and F.T. Kong, Effects of Minor Yttrium Addition on Hot Deformability of Lamellar Ti-45Al-5Nb Alloy, *T. Nonferr. Metal. Soc.*, 2007, **17**, p 58–63
32. S. Wang, L.G. Hou, J.R. Luo, J.S. Zhang, and L.Z. Zhuang, Characterization of Hot Workability in AA 7050 Aluminum Alloy Using Activation Energy and 3-D Processing Map, *J. Mater. Process. Technol.*, 2015, **225**, p 110–121
33. D.X. Wen, Y.C. Lin, J. Chen, X.M. Chen, J.L. Zhang, and Y.J. Liang, Work-Hardening Behaviors of Typical Solution-Treated and Aged Ni-Based Superalloys During Hot Deformation, *J. Alloys Compd.*, 2015, **618**, p 372–379